



Capillary instability induced gas-liquid displacement in porous media: Experimental observation and pore network model

Tao Zhang ¹, Rui Wu,^{1,2,*} C. Y. Zhao,^{1,2} Evangelos Tsotsas,³ and Abdolreza Kharaghani ³

¹*School of Mechanical Engineering, Shanghai Jiao Tong University, Shanghai 200240, China*

²*Key Laboratory for Power Machinery and Engineering, Ministry of Education, Shanghai Jiao Tong University, Shanghai 200240, China*

³*Chair of Thermal Process Engineering, Otto von Guericke University, P.O. 4120, 39106 Magdeburg, Germany*



(Received 9 March 2020; accepted 15 September 2020; published 21 October 2020; corrected 15 December 2020)

Visualization experiments and pore network models on evaporation of capillary porous media are presented in this work. We show that in a simple model porous medium the pores occupied by gas can be refilled with liquid, snapping off a gas bubble, which then moves to a stable configuration. This phenomenon, referred to as capillary instability, is induced due to heterogeneity in wettability of the pore surfaces and has a much smaller time scale compared to the evaporation process. The capillary instability is explored based on the optical images obtained from visualization experiments. The residual liquid in pores can suppress the capillary valve effect, which is induced by the sudden geometrical expansion and can hinder the movement of the gas-liquid interface. For better understanding of the capillary instability induced gas-liquid displacement, a pore network model that accounts for capillary and viscous forces as well as the inertial effect is developed. The pore network simulation results agree well with experimental data. The ratio of the square of the average meniscus moving speed predicted by the pore network model with the inertial effect to the average meniscus moving speed obtained from the model without the inertial effect is a linear function of the Weber number. When the Weber number exceeds a critical value, more pores are invaded by the gas-liquid interface in the pore network model with the inertial effect than in the model neglecting the inertial effect. The pore network model developed here opens up a route to better understand the role of inertial effects in two-phase transport in porous media.

DOI: [10.1103/PhysRevFluids.5.104305](https://doi.org/10.1103/PhysRevFluids.5.104305)

I. INTRODUCTION

Two-phase fluid transport in porous media is ubiquitous in nature and many industrial applications. This phenomenon occurs, for instance, during evaporation, where the gas-liquid interface recedes preferentially into a porous medium, and the pores initially filled with liquid are gradually occupied by the gas phase [1]. This gas-liquid interface movement is influenced by the interplay of the viscous forces, gravity, thermal gradient, pore structure, and wettability [2–6]. The gas-liquid interface movement determines the phase distribution in porous media and hence the evaporation kinetics [7]. Accurate description of gas-liquid interface movement is therefore of vital importance. Much progress, both experimentally and numerically, has been made on evaporation in porous media [8–13]. But unveiling the dynamics of gas-liquid interface movement in porous materials

*Corresponding author: ruiwu@sjtu.edu.cn

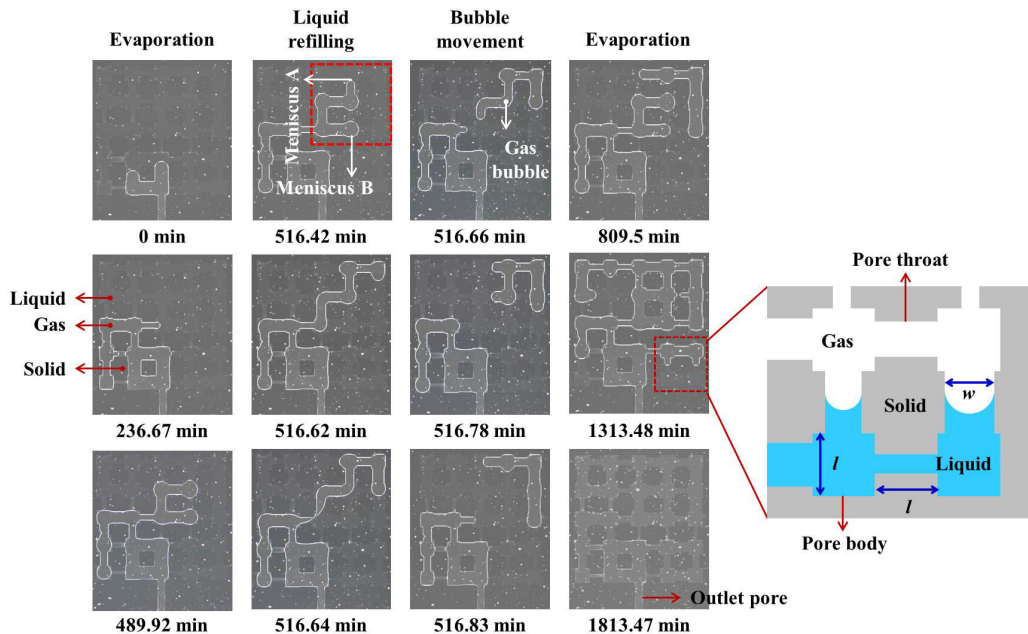


FIG. 1. Refilling of pores with liquid and bubble formation and movement observed during evaporation of a microfluidic pore network composed of pore bodies and pore throats (the pore length and width are also illustrated). The left and right columns are the evaporation process. The middle two columns are capillary instability induced liquid refilling and bubble formation and movement processes (about 40 s). Gas, liquid, and solid are shown in light gray, dark gray, and black in the experimental images, respectively.

is still a challenge. This is due to the fact that real porous materials are often opaque and have complex pore structures with nonuniform wettability of the pore surfaces.

Visualization experiments with microfluidic pore networks composed of regular pores, which enable precise visualization of the gas-liquid interface (meniscus), is proven to be a useful approach for understanding two-phase transport phenomena in porous media [14–20]. Based on the microfluidic visualization experiments, we observe surprisingly that during evaporation of a microfluidic pore network composed of cuboid pores (horizontally placed and the gravity effects can thereby be neglected), liquid refills the pores occupied by gas, snapping off a gas bubble (or gas ganglion), which then moves rapidly until a stable configuration is reached; see the middle two columns in Fig. 1. The refilling of already drained pores with liquid and bubble movement has a time scale about 30 s, which is much smaller than that associated with the whole evaporation process (about 30 h). Despite such a small time scale, the pore refilling and bubble movement, without a doubt, influences the liquid distribution in the pore network and consequently the evaporation kinetics.

The menisci movement during evaporation in porous media is similar to the drainage of a nonwetting phase displacing a wetting phase (in the evaporation case, the gas is the nonwetting phase, and the liquid is the wetting phase). For evaporation in the horizontally placed pore network shown in Fig. 1 (see the left and the right column), the movement of the menisci is slow and hence is controlled by capillary forces. As we will show later, the refilling of pores by liquid and the bubble movement in Fig. 1 is attributed to the capillary instability induced by the heterogeneity in wettability and structure of the pore network. Such capillary instability during drainage in a microfluidic pore network has been reported in Ref. [20]; however, it is not revealed the formation of ganglion of the nonwetting fluid. Formation of ganglia of nonwetting fluid has been widely observed in steady-state two-phase flow in porous media; e.g., see Refs. [21–23]. In these studies, the nonwetting and wetting fluids are simultaneously injected into the porous media, different

from the drainage case of a nonwetting phase displacing a wetting phase. The mechanism for formation of ganglia of the nonwetting fluids in the drainage (e.g., Fig. 1) and the steady-state two-phase flow in porous media therefore could be different. Although many studies have been performed on the two-phase transport in porous media, the mechanisms for formation of ganglia of the nonwetting fluids in the slow drainage process, e.g., the observed gas bubble in Fig. 1, are still unclear. Addressing this issue can definitely provide insights into the two-phase transport in porous media.

In this work, the capillary instability induced the gas-liquid displacement in the pore network shown in Fig. 1 is thoroughly investigated. This effort is made to essentially disclose, from the pore-scale perspective, the mechanisms for the formation of ganglia of the nonwetting fluid in porous media during slow drainage. Obviously, the pore-scale dynamics of the moving menisci influences the continuum-scale two-phase transport in porous media. Disclosing such influence is of great importance for developing accurate continuum models for the two-phase transport in porous media. The pore network modeling approach is an effective tool to link the menisci dynamics and the continuum-scale transport properties (for two-phase transport in porous media). This is partly due to the fact that pore network models provide a reasonable trade-off between the essential depiction of the menisci dynamics and the computational efficiency. A pore network model is developed in this work so as to provide a technique to reveal the role of the capillary instability effect in the two-phase flow in porous media. The developed pore network model takes into account not only the capillary forces, the viscous forces, the capillary valve effect, but also the inertial forces.

The inertial effects are usually neglected in the existing pore network models for two-phase transport in porous media. In few pore network studies, the inertial effect is considered only in pores with gas-liquid menisci and that is disregarded in pores fully-filled with liquid, e.g., Ref. [13]. The inertial effects are successfully considered in all liquid-filled pores in the present pore network model. The guess-and-correct method is used to solve the pressure and velocity fields in the pore network. The pore network simulations and the experimental results are in good agreement, demonstrating the effectiveness of the developed model. The developed pore network model provides a route for better understanding the role of inertial effects in two-phase transport in porous media.

In what follows, the experimental observation is explained in detail. The pore network model accounting for the inertial effect is developed and validated in Sec. III. In Sec. IV, the impacts of inertial effect on gas-liquid displacement are discussed. Summary and conclusions are presented in Sec. V.

II. EXPERIMENTS

The quasi-two-dimensional (2D) microfluidic pore network used in our experiment is fabricated by bonding a glass sheet to a silicon wafer etched with the designed pore structures. The pore network consists of 5×5 large pore bodies connected by small pore throats (Fig. 1). All pores are cuboid and have a height of $h = 50 \mu\text{m}$. In the plane perpendicular to the height direction, the pore bodies are square and have a side length of $l = 1 \text{ mm}$. The distance between the centers of two neighboring pore bodies is 2 mm. All pore throats have a length of $l = 1 \text{ mm}$, but their widths, w , vary between 0.14 and 0.94 mm. The width of each pore throat can be found in Fig. S1 in the Supplemental Material [24]. The pore network is connected to environment through an outlet pore of 2-mm long and 0.5-mm wide. The evaporation experiment is performed at the temperature of $26.5 \pm 2 \text{ }^\circ\text{C}$ and a relative humidity of $67.3 \pm 2 \%$. The pore network, initially filled with ethanol, is horizontally placed on a plate. A camera (Nikon D810) and an inverted microscope (Olympus IX73 with a 4X lens) are used to record the movement of menisci in the pore network during evaporation. The images are analyzed to determine the liquid distribution, the speed of the moving menisci, the curvature radii of menisci based on the arc fitting method [25,39–41], and the contact angle based on the polynomial fitting approach [26]. The detailed image processing procedures are presented in Figs. S2 – S4 in the Supplemental Material [24].

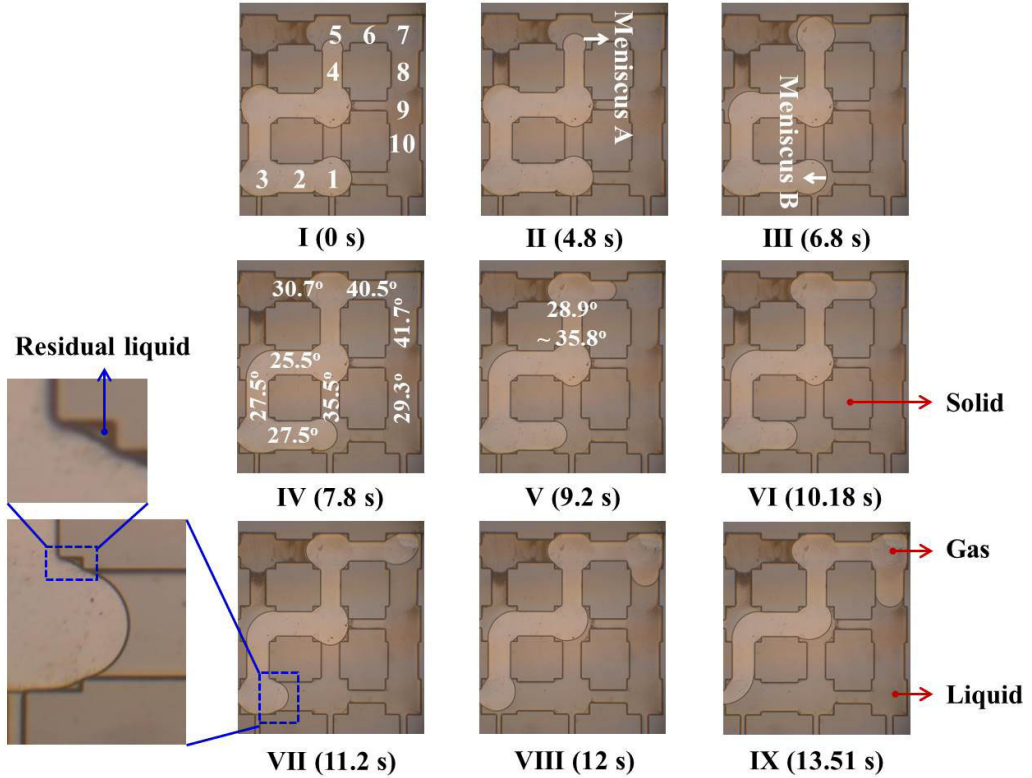


FIG. 2. Evolution of the moving menisci during capillary instability induced refilling of pores in the top right zone of the pore network (i.e., the zone marked by the red box in Fig. 1). Menisci A and B are moving, while the other menisci remain almost static. The pores that can be invaded by menisci are numbered. The contact angles of the pore throats are also shown in the images of IV and V.

The advancing and receding menisci are defined as those moving towards the liquid and gas phases, respectively. The speed of a moving meniscus in a pore is defined as the rate of liquid flow in this pore divided by the cross-sectional area of the pore body (all pore bodies have the same cross sectional area). Since the pore network structure is etched in silicon wafer in our microfluidic model, we can get the contact angle (taken in the liquid phase) for the silicon surface, θ_s , based on the image analysis. The contact angle hysteresis for the silicon surface is small and can be neglected. The contact angle for the glass surface is $\theta_g = 0^\circ$ [27].

As shown in Fig. 2 (image at stage IV), the value of θ_s is different in each pore, and varies from 25.5° to 41.7° , indicating the wettability heterogeneity of the pore surface. Nevertheless, the contact angle of an ethanol droplet on a polished silicon (smooth surface) is reported to be about 19° , and as the droplet evaporates, the contact angle can be reduced to less than 5° [28]. In Ref. [29], the contact angles of droplets of water-ethanol solutions on a silicon have been measured, and it was stated that the contact angle approaches to zero as the ethanol concentration increases. Clearly, the contact angle in the present study is significantly higher than those reported in the previous literature. Here, the contact angle is obtained by extrapolating the macroscopic fit of the in-plane (perpendicular to the thickness direction of the pore) shape of the meniscus to the pore wall. Because of the liquid film at the surface of the pore wall, the “wall surface” identified by the imaging processing can be not the real wall surface. To this end, the obtained contact angle actually is the so-called apparent contact angle [30–32]. The apparent contact angle is also dependent on the surface roughness [32]. The roughness of the pore wall is illustrated in Fig. S5 in the Supplemental Material [24]. The wall

roughness in each pore could be different due to the fabrication uncertainty. This contributes partly to explain the wettability heterogeneity of the pore network illustrated in Fig. 2. The contact angle mentioned hereafter represents the apparent contact angle unless otherwise specified.

The detailed menisci movement during refilling of pores shown in Fig. 1 (second column from the left) is presented in Fig. 2. The images in Fig. 1 are obtained by the camera (Nikon D810), which has a larger view field but a lower resolution as compared to the microscope (Olympus IX73 with a 4X lens). To understand in detail the menisci movement during the liquid refilling process, we repeat the evaporation experiment by using the microscope to get high resolution images of gas-liquid menisci in the pore network so as to get the accurate curvature radii and contact angles of menisci. The microscope cannot capture the whole zone of the pore network. Only the zone of 3×3 pore bodies at the up-right of the pore network is shown in Fig. 2. The location of the zone captured by the microscope is marked by the red box in Fig. 1. Menisci A and B shown in Fig. 2 are also illustrated in Fig. 1. The movement of menisci A and B in Fig. 2 is similar to that in Fig. 1, indicating the repeatability of the experiments.

Menisci A and B shown in Fig. 2 are the advancing and the receding menisci, respectively. The variations of speeds and curvature radii of these two menisci are depicted in Fig. 3. In Fig. 3(b), r_i is the curvature radius of the meniscus in the plane shown in Fig. 2. The value of r_i is obtained from the image analysis (see Fig. S3 in the Supplemental Material [24]). The curvature radius in the plane perpendicular to the one shown in Fig. 2 is denoted as r_h .

At stage I in Fig. 2, the meniscus A is at the entrance of pore body 5. At the interface between a pore throat and a pore body, a sudden geometrical expansion exists, which can hinder the meniscus movement, i.e., the so called capillary valve effect. More detailed explanation on the capillary valve effect can be found in Refs. [14,15]. The evolution of the meniscus A during its invasion into pore body 5 is detailed in Fig. S6 in the Supplemental Material [24]. The contact angle of meniscus A at the side wall increases suddenly from θ_s to $\theta_s + 90^\circ$ when the triple line at the side wall of pore throat 4 moves to the entrance of pore body 5. The triple line of meniscus A at the side wall is then pinned, since it cannot move toward the liquid phase until the contact angle is reduced to θ_s . On the other hand, pore throats and pore bodies have the same height; hence, the triple line at the top glass wall and the bottom silicon wall continue moving. As a result, meniscus A reshapes and thus the contact angle of meniscus A at the side wall reduces. As this contact angle decreases from $\theta_s + 90^\circ$ to 90° , the curvature radius, r_i , of meniscus A decreases. But, as the contact angle further reduces from 90° to θ_s , the curvature radius, r_i , increases, resulting in a lower capillary pressure, P_c . The capillary pressure is defined as $P_c = P_g - P_l = \sigma(1/r_i + 1/r_h)$, where σ is the surface tension, P_l is the liquid pressure, and P_g is the gas pressure. Since P_g is constant during evaporation, the lower the capillary pressure, the higher the liquid pressure. The increase of liquid pressure at meniscus A results in higher liquid pressure in the pore network. The increased liquid pressure can lead some other menisci in the pore network to be unstable, e.g., meniscus B in Fig. 2. A meniscus is unstable when $P_l - P_g$ across the meniscus is larger than the threshold pressure for the meniscus to refill the pore occupied by the gas phase. A meniscus cannot invade into a pore when the pressure difference in the invading and displaced phases across this meniscus is smaller than the threshold pressure of the pore. The instability of meniscus B is induced by the variation of the capillary force of the advancing meniscus A. We call this the capillary instability. This capillary instability effect is the reason for the pore refilling and the bubble formation and movement shown in Fig. 1.

The movement of menisci A and B in Fig. 2 depends on the difference between the liquid pressures at these two menisci, $P_{l,A} - P_{l,B}$. Based on the definition of the capillary pressure, the value of $P_{l,A} - P_{l,B}$ is determined as

$$P_{l,A} - P_{l,B} = \sigma \left(\frac{1}{r_{i,B}} - \frac{1}{r_{i,A}} \right) + \sigma \left(\frac{1}{r_{h,B}} - \frac{1}{r_{h,A}} \right). \quad (1)$$

Equation (1) indicates that the movement of menisci relies on the curvature radii, r_i and r_h . For instance, from stages II to III shown in Fig. 2, the speeds of the moving menisci are always

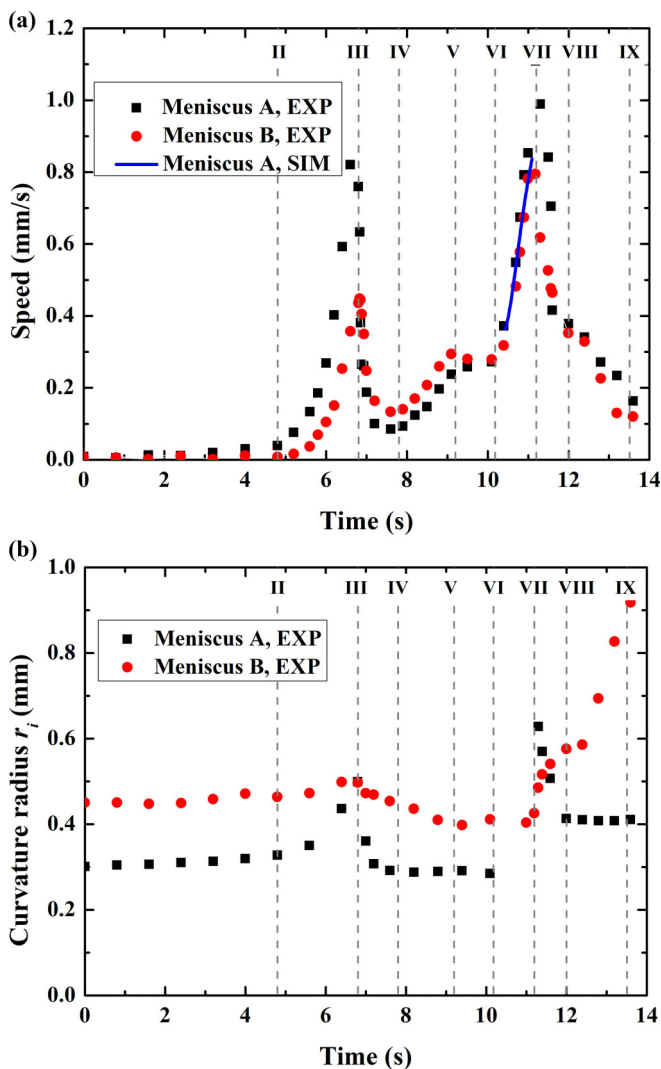


FIG. 3. Variation of (a) menisci speeds and (b) curvature radii r_i , during refilling of pores shown in Fig. 2. Menisci A and B as well as various evaporation stages are illustrated in Fig. 2. The blue line in (a) is gained from pore network simulations.

increasing as meniscus A enters the pore body 5, Fig. 3(a). The higher speed is owing to the increased $r_{i,A}$ [Fig. 3(b)], which in turn results in the increased $P_{l,A}-P_{l,B}$, Eq. (1). However, as shown in Fig. 3(b), $r_{i,A} < r_{i,B}$ from stages I to III. If menisci A and B have the same value of r_h , then $P_{l,A}-P_{l,B} < 0$, Eq. (1), and the capillary instability induced gas-liquid displacement shown in Fig. 1 will not occur. From this point of view, it should be that $r_{h,A} > r_{h,B}$.

During stages I to III shown in Fig. 2, both menisci A and B are in the pore bodies, and the triple lines at the side walls are pinned at the entrance of the pore bodies and are not moving. Hence, no corner liquid films form when these two menisci advance in the pore bodies. For this reason, r_h can be expressed as $r_h = h/(1 + \cos\theta_s)$, and the effects of the corner liquid films on the capillary pressure, e.g., Ref. [30], is not considered. As a result, to get $r_{h,A} > r_{h,B}$, the contact angle, θ_s , of pore body 5 should be larger than that of pore body 1. Nevertheless, it is not easy to obtain the values of θ_s in the pore bodies, since we cannot observe the moving triple line along the side walls of pore

bodies. By contrast, we can get the values of θ_s in the pore throats. As shown in Fig. 2 (image at stage IV), pore throats have different values of θ_s .

When a meniscus in a pore throat, e.g., meniscus A in pore throat 6 and meniscus B in pore throat 2 shown in image V in Fig. 2, the capillary pressure for this meniscus shall be affected by the corner liquid films, since the lengths of the corner liquid films vary as the meniscus moves. To this end, r_h in Eq. (1) cannot be expressed simply as $r_h = h/(1 + \cos\theta_s)$. To calculate the capillary pressure for a meniscus in a pore with corner liquid films, two methods can be exploited. The first is the Mayer and Stowe-Prince (MS-P) method [33,34]. In the second method proposed by Wong *et al.* [30], the shape of the meniscus in the pore is determined, from which the capillary pressure is obtained. The results obtained by these two methods are almost the same; see Refs. [30,35]. The MSP method is more convenient for calculation, and therefore is employed to determine the capillary pressure in the pore network model developed in Sec. III; see Eq. (5).

If pore throats 2 and 6 have the same contact angle, then the capillary pressure determined by Eq. (5) is larger for meniscus A in pore throat 6 than for meniscus B in pore throat 2. For instance, if the contact angle is 0° , the capillary pressure is 947.1 Pa for meniscus A and 926.9 Pa for meniscus B. This indicates that liquid pressure at meniscus B is larger than that at meniscus A, and the capillary stability induced gas-liquid displacement cannot occur. By contrast, if the measured apparent contact angle (see Fig. 2) is used for pore throats 2 and 6, then the capillary pressure for meniscus A in pore throat 6 (834.5 Pa) is lower than that for meniscus B in pore throat 2 (876.2 Pa), which implies that meniscus A advances and meniscus B recedes, consistent with the experimental observation.

Hence, the capillary instability induced two-phase displacement observed in the present study could be attributed to the wettability heterogeneity of the pore network. The wettability of the pore surface can be essentially reflected by the measured apparent contact angle. Since r_h in Eq. (1) cannot be expressed simply as $r_h = h/(1 + \cos\theta_s)$ when the meniscus is in the pore throat (because of the corner liquid films), we focus on the measured r_i in the following analysis so as to illustrate the variation of the meniscus shape during the capillary instability induced gas-liquid displacement shown in Fig. 2.

At stage III shown in Fig. 2, meniscus A touches the side wall of the pore body 5 as well as the entrance of pore throat 6. After this, meniscus B continues to move in pore body 1, and meniscus A enters pore throat 6, stage IV of Fig. 2. From stages III to IV, $r_{i,A}$ reduces significantly as meniscus A enters pore throat 6 from pore body 5, whereas, the decrease of $r_{i,B}$ is smaller, Fig. 3(b). As a result, $P_{l,A} - P_{l,B}$ decreases, Eq. (1), leading to the reduced menisci moving speed, Fig. 3(a).

After meniscus A invades pore throat 6, meniscus B continues invading the gas phase in pore body 1 until it enters the pore throat 2, stage V in Fig. 2(a). During this process, $r_{i,A}$ remains constant, and $r_{i,B}$ reduces, Fig. 3(b), thereby leading to increased $P_{l,A} - P_{l,B}$, Eq. (1). Hence, the speeds of the moving menisci become higher, Fig. 3(a). From stages V to VI, both menisci A and B are in pore throats. Therefore, variations of curvature radii and speeds of moving menisci are trivial, Fig. 3.

After stage VI, meniscus A invades pore body 7 from pore throat 6; see stage VII in Fig. 2. During this process, $r_{i,A}$ increases due to the capillary valve effect; the value of $r_{i,A}$ is not shown in Fig. 3(b), since the shape of meniscus A, as shown in stage VII of Fig. 2, is not a circle due to the contaminant in pore body 7. Meniscus B is always in pore throat 2 from stages VI to VII, and $r_{i,B}$ is almost constant, Fig. 3(b). As a result, $P_{l,A} - P_{l,B}$ increases, Eq. (1), leading to higher speeds of moving menisci, Fig. 3(a).

After stage VII, meniscus A invades pore throat 8 and meniscus B enters pore body 3, stage VIII in Fig. 2. During this process, $r_{i,A}$ decreases and $r_{i,B}$ increases, resulting in the decreased $P_{l,A} - P_{l,B}$, Eq. (1), and hence the speeds of the moving menisci reduce, Fig. 3. After the stage VIII shown in Fig. 2, meniscus B connects two gas-filled pore throats connected to pore body 3, and $r_{i,B}$ increases as the liquid saturation in the pore body increases. By contrast, $r_{i,A}$ is almost constant, Fig. 3(b). Although $r_{i,A} < r_{i,B}$ at the stage VIII, meniscus B continues refilling of pore body 3; see stage IX in Fig. 2. When pore body 3 is completely filled by liquid, a gas bubble is formed in the pore network, Fig. 1.

During meniscus B entering pore body 3 from pore throat 2 (from stages VII to VIII shown in Fig. 2), we find that the influence of the capillary valve effect induced by the sudden geometrical expansion between the pore throat and the pore body is trivial. The capillary valve effect is suppressed by the residual liquid in pore body 3. The detailed formation of the residual liquid in a pore body and the invasion of meniscus B into pore body 3 from pore throat 2 are presented, respectively, in Figs. S7 and S8 in the Supplemental Material [24]. Before meniscus B invades pore body 3, the intersectional points between pore throat 2 and pore body 3 are attached to the residual liquid. As the triple lines (at the side walls) of meniscus B move to these intersectional points, meniscus B will merge with the residual liquid to form a new meniscus. During this process, meniscus B keeps concave towards the gas phase.

For the capillary instability induced gas-liquid displacement shown in Fig. 2, menisci A and B interact with each other through the liquid filled pores. The menisci movement in this case is called the one induced by the capillary instability with pore flow. We also observe in the experiment that the two menisci interact with each other through the corner liquid films, i.e., the menisci movement induced by the capillary instability with corner flow; see Fig S9 in the Supplemental Material [24]. The speed of the moving menisci due to the capillary instability with the corner flow is much smaller than that with the pore flow. It has been revealed that the speed of the capillary instability induced advancing meniscus depends on the number of interacting receding menisci [20]. Here we reveal that the speed of moving menisci induced by the capillary instability also depends on the flow pattern between the interacting menisci.

The corner liquid films also can influence the invasion of a meniscus from a pore throat to a pore body. During the meniscus invasion into pore body 3 from pore throat 2 shown in Fig. 2, the residual liquid in the pore body is always connected to the mouth of the pore throat. We also observe in the experiment that when a meniscus in a pore throat reaches the intersectional points between the pore throat and the adjacent pore body, the residual liquid in the pore body can be not attached to the mouth of the pore throat; see Fig S10 in the Supplemental Material [24]. Owing to the presence of corner liquid films, the meniscus in the pore throat and the residual liquid in the pore body are actually connected and can interact with each other. During invasion of the meniscus from the pore throat to the pore body, the liquid pressure at the meniscus will increase due to the capillary valve effect, which in turn results in the growth of the residual liquid because of the presence of the corner liquid films. When the residual liquid grows to touch the mouth of the pore throat, the meniscus is still concave towards the gas phase; see Fig S10 in the Supplemental Material [24]. Then the meniscus will keep concave as it enters the pore body, similar to the invasion process shown in Fig. S8 in the Supplemental Material [24].

To understand the role of the corner liquid films in the meniscus invasion into a pore body from a pore throat, we compare schematically the invasion processes in the cases with and without corner liquid films in Fig. S11 in the Supplemental Material [24]. In the case with the corner liquid films in the pores and the residual liquid in the pore body, the meniscus keeps concave towards the gas phase as it invades the pore body from the pore throat, as we discussed above. By contrast, in the case without the corner liquid films, the residual liquid in the pore body (if it exists) is not connected to the invading meniscus. To this end, the meniscus has to change from concave to convex (towards the gas phase) during its invasion into the pore body, attributed to the capillary valve effect. Hence, the threshold pressure for the meniscus to invade the pore body is larger in the case without the corner liquid films than in the case with the corner liquid films. If there were no corner liquid films in the pores and no residual liquid in the pore bodies in the pore network in our experiment, the capillary instability induced receding menisci will not invade the gas-filled pore body (because of the capillary valve effect), and the bubble shown in Fig. 1 will not form.

To form the gas bubble shown in Fig. 1, an empty pore body connected to at least two empty pore throats must be refilled completely by the liquid (an empty pore is the one occupied by gas), e.g., the central pore body in Fig. 1 (i.e., pore body 3 in Fig. 2). The refilling of a pore body with liquid is affected by the state (empty or filled) of the connected pore throats, as illustrated in Fig. 4. A filled pore is the one filled with liquid. For an empty pore body connected to three filled pore

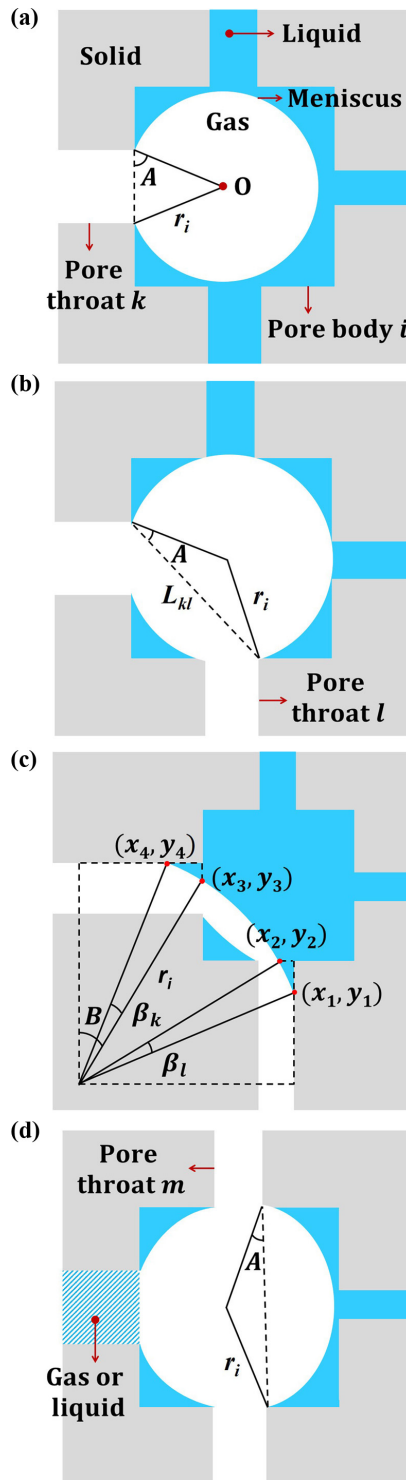


FIG. 4. Schematic of the meniscus configuration in a partially filled body i with (a) only one adjacent empty pore throat k ; (b) and (c) two adjacent empty pore throats k and l neighboring to each other, and (d) two adjacent empty pore throats l and m opposite to each other.

throats and one empty pore throat [Fig. 4(a)], the gas-liquid meniscus can remain concave towards the gas phase during refilling of a pore body, e.g., pore body 1 in Fig. 2.

For an empty pore body connected to two filled pore throats neighboring to each other and two empty pore throats [Figs. 4(b) and 4(c)], the meniscus also can remain concave towards the gas phase during refilling of the pore body; but the curvature radius can increase to a large value; see refilling of the central pore body in Fig. 1 (i.e., pore body 3 in Fig. 2). For an empty pore body connected to two empty pore throats opposite to each other [Fig. 4(d)], the meniscus will change from concave to convex (towards the gas phase) in order to invade the pore body, mainly attributed to the capillary valve effect induced by the sudden geometrical expansion between the pore body and the two empty pore throats.

Our experimental studies show that during slow drainage in a porous medium, the increase of the curvature radius of the advancing meniscus (which displaces the wetting phase) can lead some other menisci to be unstable and hence to recede towards the nonwetting phase. The movement of the advancing and the receding menisci depends on not only the interplay between them (e.g., the flow pattern between them), but also the pore structure, wettability, and state (e.g., the capillary valve effect, the wettability heterogeneity, the corner films, number of adjacent pore throats filled with the wetting phase, and the residual wetting phase in the pore body). The main driving force for the capillary instability induced two-phase flow is the difference in the capillary forces between the advancing and the receding menisci, which is induced by the wettability heterogeneity in the pore network in the present study. The difference in the capillary forces between the advancing and receding menisci can also be attributed to the structural heterogeneity in the pore network; see the capillary instability induced gas-liquid displacement during evaporation in a pore network composed of a large pore zone and a small pore zone in Fig. S12 in the Supplemental Material [24]. It has been revealed that a gas bubble can also be formed by swelling of the corner films during evaporation in a composite pore network [36].

To form the gas bubble in the pore network shown in Fig. 1, a gas (nonwetting phase) occupied pore body connected to at least two empty pore throats must be refilled completely by the liquid (wetting phase). This refilling of the pore body depends on the competition between the driving force for the movement of the receding menisci and the threshold pressure for the liquid to refill the pore body. Both the driving force and the pore threshold pressure depend on the wettability of the pore.

In the present study, we repeat the evaporation experiments four times. The first two experiments are performed with camera; in these two experiments, gas bubble formation is always observed. Then, we repeat the experiment twice by using the microscope to get images of high resolution so as to get the detailed evolution of the moving menisci in the pore network; however, the gas bubble formation is not observed, even though the capillary instability induced refilling of pores always occurs, Fig. 2. The reason could be that after the first two experiments, the pore network is contaminated, and the wettability of the pore is altered; see Fig. S13 in the Supplemental Material [24] for more details. Refilling of the pores observed in the experiments with the camera and the microscope are almost the same (comparing Figs. 1 and 2), indicating that the change of the wettability of the pore network after the first two experiments could be small. But, if the driving force for the movement of the receding menisci and the threshold pressure to refill the central pore body in the pore network (i.e., pore body 3 in Fig. 2) are comparable, then even a small variation in the pore wettability can change their relative order and hence affects the formation of the gas bubble. When receding meniscus B refills the pore body 3 in Fig. 2, the advancing meniscus A invades the pore body 9. As shown in Fig. 2, the pore throats adjacent to pore body 2 have similar contact angles; whereas pore throats 8 and 10 adjacent to pore body 9 have different contact angles, indicating that the wettability of pore body 9 is not uniform. To this end, even a small change of the wettability distribution could affect significantly the capillary pressure of the meniscus in pore body 9 and hence the driving force. From this point of view, it is necessary to consider the variation of the surface wettability so as to understand in detail the dynamics of the capillary instability induced two-phase displacement in porous media.

For the quasi-2D pore network used in the experiment, the coordination number of each pore body is 4, which may be less than that in 3D porous media. More than two menisci can be interplayed with each other in a 3D porous medium, much more complex than the interaction of two menisci in the quasi-2D pore network revealed in the present study. In spite of this, we conjecture that the underlying mechanisms for menisci movement in the 2D and 3D pore networks should be similar. Since it is not easy to observe directly the interplay between the menisci in a 3D porous medium, an alternative is to exploit the pore network modeling approach. It is of vital importance to develop a pore network model that can accurately describe the movement of the menisci. Although the 2D pore network cannot represent the 3D porous media, the mechanism for the two-phase displacement revealed by the 2D microfluidic experiment guides the development of the pore network model presented in the following section.

III. PORE NETWORK MODEL

In the present pore network model, the inertial forces are considered for flow in all liquid-filled pores. The gas pressure is assumed constant. In addition, the capillary forces, liquid viscous forces, and capillary valve effect are also taken into account in the model.

The liquid flow in a pore is taken as a 1D fully developed laminar flow. A filled pore is the one with the local liquid saturation $s_l > 0$ in pore throats or $s_l > s_{l,re}$ in pore bodies. Here $s_{l,re}$ is the saturation of the residual liquid. To determine $s_{l,re}$, we assume that the residual liquid in a pore body connects the mouths of two pore throats, and its shape is a triangle. A partly filled pore ($s_l \leq 1$) contains menisci and has at least one adjacent empty pore, while a fully filled pore ($s_l = 1$) is surrounded by filled pores. The empty pore is the one with $s_l = 0$ for pore throats or $s_l = s_{l,re}$ for pore bodies.

The liquid flow in a filled pore throat k between two filled pore bodies, i and j , can be described as

$$\frac{\partial [hw_k \rho_l (\frac{l_i}{2} + l_k + \frac{l_j}{2}) v_{l,k}]}{\partial t} = (P_{l,i} - P_{l,j}) hw_k - g_k \left(\frac{l_i}{2} + l_k + \frac{l_j}{2} \right) v_{l,k}, \quad (2)$$

where ρ_l is the liquid density, μ_l the dynamic viscosity, v_l the liquid velocity, and g_k is expressed as [37]

$$g_k = \frac{\pi^4 \mu_l}{8 \left[1 - \frac{2h}{\pi w_k} \tanh\left(\frac{\pi w_k}{2h}\right) \right]} \frac{w_k}{h}. \quad (3)$$

The pore width and length are depicted in Fig. 1. The liquid flow in a filled pore throat k with $s_{l,k} < 1$ from a filled pore body i to an empty pore body j is depicted as

$$\rho_l hw_k \left\{ \left(\frac{l_i}{2} + s_{l,k} l_k \right) \frac{d^2(s_{l,k} l_k)}{dt^2} + \left[\frac{d(s_{l,k} l_k)}{dt} \right]^2 \right\} = (P_{l,i} - P_{l,k}) hw_k - g_k \left(\frac{l_i}{2} + s_{l,k} l_k \right) \frac{d(s_{l,k} l_k)}{dt}. \quad (4)$$

The liquid pressure in a partly filled pore is determined as $P_l = P_g - P_c$, for which the gas pressure P_g is constant. The capillary pressure, P_c , for a moving meniscus in a pore throat i is gained by the MSP method [33,34]:

$$P_c = \frac{\sigma(k_1 + 2k_2 k_4)}{w_i h - 2k_3 k_4^2}, \quad (5a)$$

$$k_1 = (2h + w_i) \cos \theta_{s,i} + w_i, \quad (5b)$$

$$k_2 = \pi - 3\theta_{s,i} - (2 \cos \theta_{s,i} - 3 \sin \theta_{s,i} + 2) \cos \theta_{s,i}, \quad (5c)$$

$$k_3 = \cos^2 \theta_{s,i} + \cos \theta_{s,i} - \frac{3 \sin \theta_{s,i} \cos \theta_{s,i}}{2} - \frac{\pi}{2} + \frac{3\theta_{s,i}}{2}, \quad (5d)$$

$$k_4 = \frac{-2k_1 k_3 + \sqrt{4k_1^2 k_3^2 - 8k_2^2 k_3 w h}}{4k_2 k_3}. \quad (5e)$$

The detailed derivation of Eq. (5) can be found in Ref. [38].

The capillary pressure for a meniscus in a partly filled pore body depends on the shape of the meniscus

$$P_c = \sigma \left(\frac{1}{r_i} + \frac{1}{r_h} \right), \quad (6)$$

for which $r_h = h/(1 + \cos\theta_s)$, whereas r_i depends on not only the liquid saturation of the pore body but also the state (empty or filled) of the adjacent pore throat. For a partly filled pore body i with only one adjacent empty pore throat [e.g., pore throat k in Fig. 4(a)], the curvature radius and the liquid saturation are

$$r_i = \frac{w_k}{2 \cos A}, \quad (7a)$$

$$s_{l,i} = 1 - \frac{r_i^2 \sin(\pi - 2|A|) \frac{A}{|A|} + (\pi + 2A)r_i^2}{2l_i^2}, \quad (7b)$$

where A is the angle shown in Fig. 4(a). The contact angle A is positive when the angle between the meniscus and the wall of the pore body is equal to or smaller than 90° , and negative when this angle is larger than 90° .

For a partly filled pore body i with two adjacent empty pore throats neighboring to each other [e.g., pore throats k and l in Fig. 4(b)], the curvature radius and the liquid saturation are

$$r_i = \frac{L_{kl}}{2 \cos A}, \quad (8a)$$

$$s_{l,i} = 1 - \frac{L_k L_l}{2l_i^2} - \frac{L_{kl}^2 \tan A}{4l_i^2} - \frac{\pi + 2A}{2l_i^2} r_i^2 + \frac{1}{8l_i^2} (l_p - W_l)(l_p - W_k), \quad (8b)$$

where $L_k = W_k/2 + l_p/2$, $L_l = W_l/2 + l_i/2$, $L_{kl} = \sqrt{L_k^2 + L_l^2}$, and A the contact angle shown in Fig. 4(b). In Fig. 4(b), the meniscus in the pore body is connected to the mouths of two pore throats. As liquid in the pore body increases, the shape of the meniscus changes. When the contact angle between the gas-solid interface of an empty pore throat and the meniscus reaches to $\pi - \theta_s$, the meniscus starts to enter this pore throat, as illustrated in Fig. 4(c). If the meniscus first enters the pore throat l , the curvature radius and the liquid saturation are

$$r_i = \frac{W_l + l_p}{2[\cos\theta_{s,l} + \cos(2A - \theta_{s,l})]}, \quad (9a)$$

$$s_{l,i} = \frac{I_p - I_{l,l}}{l_p^2}, \quad (9b)$$

$$\begin{aligned} I_p = & \frac{1}{2} [r_i \cos\theta_{s,l} + r_i \cos(2A - \theta_{s,l})] [r_i \sin(2A - \theta_{s,l}) - r_i \sin\theta_{s,l}] \\ & - \frac{1}{2} [(\pi - 2A)r_i^2 - r_i^2 \sin(2A)] \\ & + \frac{1}{8} (W_l + l_i)(l_i - W_k) + \frac{1}{2} l_i(l_i - W_l) + \frac{1}{8} (l_i - W_l)(l_i - W_k), \end{aligned} \quad (9c)$$

$$I_{l,l} = \frac{r_i^2 \sin\beta_l}{2} + \frac{|x_1 - x_2||y_1 - y_2|}{2} - \frac{\beta_l r_i^2}{2}, \quad (9d)$$

$$(x_1, y_1) = (r_i \cos\theta_{s,l}, r_i \sin\theta_{s,l}), \quad (9e)$$

$$(x_2, y_2) = (\sqrt{r_i^2 - y_2^2}, r_i \sin(2A - \theta_{s,l}) - (l_i + W_k)/2), \quad (9f)$$

$$\beta_l = \arccos \left[1 - \frac{(x_1 - x_2)^2}{2r_i^2} - \frac{(y_1 - y_2)^2}{2r_i^2} \right], \quad (9g)$$

When the meniscus enters both pore throats l and k , the curvature radius and the liquid saturation are

$$r_i = \frac{W_l + l_i}{2[\cos \theta_{s,l} + \cos B]}, \quad (10a)$$

$$s_{l,i} = \frac{I_p - I_{t,l} - I_{t,k}}{l_i^2}, \quad (10b)$$

$$I_p = \frac{1}{2}(r_i \cos \theta_{s,l} - r_i \sin \theta_{s,k})(r_i \cos \theta_{s,k} - r_i \sin \theta_{s,l}) - \frac{1}{2}[(\pi - \theta_{s,l} - \theta_{s,k})r_i^2 - r_i^2 \sin(\theta_{s,l} + \theta_{s,k})] \\ + \frac{1}{4}(W_l + l_i)(l_i - W_k) + \frac{1}{2}l_i(l_i - W_l) + \frac{1}{8}(l_i - W_l)(l_i - W_k), \quad (10c)$$

$$I_{t,k} = \frac{r_i^2 \sin \beta_k}{2} + \frac{|x_3 - x_4||y_3 - y_4|}{2} - \frac{\beta_k r_i^2}{2}, \quad (10d)$$

$$(x_3, y_3) = \left(r_i \cos \theta_{s,l} - \frac{l_i + W_l}{2}, \sqrt{r_i^2 - x_3^2} \right), \quad (10e)$$

$$(x_4, y_4) = (r_i \sin \theta_{s,k}, r_i \cos \theta_{s,k}), \quad (10f)$$

$$\beta_k = \arccos \left[1 - \frac{(x_3 - x_4)^2}{2r_i^2} - \frac{(y_3 - y_4)^2}{2r_i^2} \right], \quad (10g)$$

where B is the angle between the vertical line through the center of the meniscus and the line connecting the center and the intersectional point between meniscus and vertical side wall of the pore body, as illustrated in Fig. 4(c). The meniscus will leave the pore body and enters pore throat l and k when the curvature radius of the meniscus reaches

$$r_i = \frac{-b - \sqrt{b^2 - 4ac}}{2a}, \quad (11a)$$

$$a = 1 - \cos^2 \theta_{s,l} - \cos^2 \theta_{s,k}, \quad (11b)$$

$$b = 2W_l \cos \theta_{s,l} + (l_i + W_k) \cos \theta_{s,k}, \quad (11c)$$

$$c = -W_l^2 - \left[\frac{(l_i + W_k)}{2} \right]^2. \quad (11d)$$

For a partly filled pore body i with two adjacent empty pore throats opposite to each other [e.g., pore throats l and m in Fig. 4(d)],

$$r_i = \frac{A}{|A|} \frac{L_{lm}}{2 \cos(A)}, \quad (12a)$$

$$s_{l,i} = \frac{(l_i - \frac{W_m + W_l}{2})}{2l_i} - \frac{A}{|A|l_i^2} \left(\frac{(\pi - |2A|)r_i^2}{2} - \frac{r_i^2}{2} \sin|2A| \right) \\ + \frac{(l_i - W_k)(l_i - W_m)}{8l_i^2} + \frac{(l_i - W_l)(l_i - W_k)}{8l_i^2}, \quad (12b)$$

where contact angle A is positive when the meniscus is concave towards the liquid phase but negative when the meniscus is convex.

Based on the mass conservation law, the following equation is applied to the fully filled pore body:

$$\sum A_j v_{l,j} = 0, \quad (13)$$

where A_j is the cross-sectional area of the adjacent pore throats and $v_{l,j}$ is the liquid velocity from the pore throat to the pore body. For a partly filled pore body

$$\sum A_j v_{l,j} + \frac{dV_{l,i}}{dt} = 0, \quad (14)$$

where $V_{l,i}$ is the volume of liquid in the pore body.

The procedure to simulate the capillary instability induced gas-liquid displacement in the pore network is summarized below as well as in Fig. S14 in the Supplemental Material [24]:

- (1) The liquid saturation, velocity, and pressure in each filled pore at time t are given.
- (2) The volume of liquid, V_l , in each partly filled pore with an active meniscus (i.e., the moving meniscus) at time $t + \Delta t$ is determined. Here, $\Delta t = 1.7 \times 10^{-4}$ s is the step time. The liquid volume of a partially filled pore throat j adjacent to a filled pore body i is updated as

$$V_{l,j}^{t+\Delta t} = hw_j l_j s_{l,j}^{t+\Delta t}, \quad (15a)$$

$$(s_{l,j}^{t+\Delta t})^2 = \frac{2hw_j}{l_j^2 g_j} \left\{ (P_{l,i}^t - P_{l,j}^t) \Delta t + \frac{\rho_l}{g_j} [(P_{l,i}^t - P_{l,j}^t) hw_j - g_j s_{l,j}^t l_j v_{l,j}^t] \left(e^{\frac{-g_j \Delta t}{\rho_l hw_j}} - 1 \right) \right\} + (s_{l,j}^t)^2. \quad (15b)$$

If the updated liquid volume in the pore throat j , $V_{l,j}^{t+\Delta t}$, is negative, then the liquid volume in the adjacent filled pore body i is $V_{l,i}^{t+\Delta t} = V_{l,i}^{t+\Delta t} + V_{l,j}^{t+\Delta t}$ and $V_{l,i}^{t+\Delta t}$ is set to be zero. If $V_{l,j}^{t+\Delta t}$ is larger than the volume of the pore throat j , V_j , then the liquid volume in the adjacent empty or partially filled pore body k is $V_{l,k}^{t+\Delta t} = V_{l,k}^t + V_{l,j}^{t+\Delta t} - V_j$, and $V_{l,j}^{t+\Delta t}$ is set to be V_j .

The volume of liquid in a partly filled pore body i adjacent to a filled pore throat j is updated as

$$V_{l,i}^{t+\Delta t} = V_{l,i}^{t+\Delta t} + \sum A_j v_{l,j}^t \Delta t. \quad (16)$$

If the updated liquid volume in the pore body i , $V_{l,i}^{t+\Delta t}$, is smaller than the volume of the residual liquid $V_{rel,i}$, then the liquid volume in the adjacent filled pore throat j with the lowest capillary pressure is $V_{l,j}^{t+\Delta t} = V_{l,j}^t - (V_{rel,i} - V_{l,i}^{t+\Delta t})$, and $V_{l,i}^{t+\Delta t}$ is set to be $V_{rel,i}$. If $V_{l,i}^{t+\Delta t}$ is larger than the volume of pore body i , V_i , then the liquid volume in each adjacent empty pore throat j is $V_{l,j}^{t+\Delta t} = V_{l,j}^t + (V_{l,i}^{t+\Delta t} - V_i)/n_t$, and $V_{l,i}^{t+\Delta t}$ is set to be V_i . Here, n_t is the number of adjacent empty pore throats.

Based on the volume of liquid in each pore, the liquid saturation of each filled pore at time $t + \Delta t$ is calculated straightforwardly.

- (3) The state of each meniscus (i.e., the gas-liquid interface) is determined. A static meniscus is the one that cannot move, and an active meniscus is movable.

For each partly filled pore throat with an active meniscus and $s_l < 0.1$ or > 0.9 , if the liquid flow direction therein is different at time t and $t - \Delta t$, then the meniscus in this partly filled pore throat is labeled as static at time $t + \Delta t$ so as to avoid the numerical error. The explanation is as follows. For instance, as shown in Fig. S15a in the Supplemental Material [24], a meniscus in a partly filled pore throat is invading a neighboring empty pore body at time $t - \Delta t$. At time t , the meniscus enters the pore body, and the partly filled pore throat becomes fully filled. However, the liquid pressure in the fully filled pore throat can be smaller than the liquid pressure in the pore body. To this end, the meniscus in the pore body may recede to the mouth of the filled pore throat, leading to the change of the direction of the liquid flow in the filled pore throat. But, owing to the different curvature radii of the meniscus in the pore body and the pore throat, $P_g - P_l$ across the meniscus can be smaller than the capillary pressure of a moving meniscus in the pore throat. Hence the meniscus cannot recede into the pore throat and will stop at the mouth of the pore throat. For this reason, this meniscus is set to be static at time $t + \Delta t$. After liquid saturation update at time $t + \Delta t$, the liquid saturation in the pore throat is smaller than 1, but larger than 0.9 (actually close to 1), owing to the small time step.

Similarly, as shown in Fig. S15b in the Supplemental Material [24], when a meniscus in the partly filled pore throat invades a filled pore body, it can first enter the pore body and then recede (the liquid flow direction in the pore throat is changed), and finally stop at the mouth of the pore throat with the liquid saturation being close to 0 (not more than 0.1). As a result, if the liquid flow direction in a partly filled throat with active meniscus and $s_l < 0.1$ (or $s_l > 0.9$) is changed in the last two time steps, the meniscus is set to be static, and the liquid saturation in the pore throat is set to $s_l = 0$ (or $s_l = 1$).

For a partly filled pore throat with $s_l = 1$ and a static meniscus, if the $P_g - P_l$ across the meniscus is larger than the capillary pressure of the moving meniscus in the pore throat or smaller than the capillary pressure in the adjacent empty pore body with $s_l = s_{l, re}$, then the static meniscus is set to be active. For a partly filled pore body with $s_l = 1$ and a static meniscus attached to an empty pore throat, if the $P_g - P_l$ across the meniscus is smaller than the capillary pressure of the moving meniscus in the connected pore throat or larger than the capillary pressure in the pore body when the contact angle between the meniscus and the wall surface is right (the capillary pressure at this moment is the largest because of the capillary valve effect), then the static meniscus is set to be active.

(4) The liquid and gas clusters in the pore network are identified.

(5) The liquid pressure and velocity in each filled pore are determined by the following guess-and-correct method.

(5.1) The pressures of liquid in the partially filled pore with active menisci, $P_l^{t+\Delta t}$, are determined by the capillary pressure, Eqs. (5)–(12). For the partly filled pore throat with static menisci, the liquid velocity, $v_l^{t+\Delta t}$, is zero. The pressures of liquid in the fully filled pore are guessed as $P_l^{*, t+\Delta t}$.

(5.2) Based on the guessed liquid pressure field, the guessed liquid velocity in each fully filled pore throat, e.g., pore throat k connecting pore bodies i and j , is determined by solving Eq. (2):

$$v_{l,k}^{*,t+\Delta t} = \frac{(P_{l,i}^{*,t+\Delta t} - P_{l,j}^{*,t+\Delta t})\Delta t h w_k + h w_k \rho_l \left(\frac{l_i}{2} + l_k + \frac{l_j}{2}\right) v_{l,k}^t}{h w_k \rho_l \left(\frac{l_i}{2} + l_k + \frac{l_j}{2}\right) + \Delta t g_k \left(\frac{l_i}{2} + l_k + \frac{l_j}{2}\right)}. \quad (17)$$

The guessed liquid velocity in the partly filled pore throat with an active meniscus, e.g., pore throat k connected to filled pore body i , is gained by solving Eq. (4) analytically

$$v_{l,k}^{*,t+\Delta t} = \frac{1}{g_k l_k s_{l,k}^{t+\Delta t}} \left\{ (P_{l,i}^{*,t+\Delta t} - P_{l,k}^{t+\Delta t}) h w_k + [(P_{l,i}^{*,t+\Delta t} - P_{l,k}^{t+\Delta t}) - g_k l_k s_{l,k}^t v_{l,k}^t] e^{\frac{-g_k \Delta t}{\rho_l h w_k}} \right\}. \quad (18)$$

In Eqs. (17) and (18), if the pore body is the partly filled pore with active menisci, then $P_l^{*, t+\Delta t} = P_l^{t+\Delta t}$.

(5.3) The correct liquid pressure and velocity are defined as $P_l^{t+\Delta t} = P_l^{*, t+\Delta t} + P_l'$ and $v_l^{t+\Delta t} = v_l^{*, t+\Delta t} + v_l'$, respectively. Here, P_l' is the liquid pressure correction, and v_l' is the liquid velocity correction. It should be noted that the correct liquid pressure and velocity also satisfy Eqs. (2) and (4), and the following equations can be gained:

$$v_{l,k}^{t+\Delta t} = \frac{(P_{l,i}^{t+\Delta t} - P_{l,j}^{t+\Delta t})\Delta t h w_k + h w_k \rho_l \left(\frac{l_i}{2} + l_k + \frac{l_j}{2}\right) v_{l,k}^t}{h w_k \rho_l \left(\frac{l_i}{2} + l_k + \frac{l_j}{2}\right) + \Delta t g_k \left(\frac{l_i}{2} + l_k + \frac{l_j}{2}\right)}, \quad (19)$$

$$v_{l,k}^{t+\Delta t} = \frac{1}{g_k l_k s_{l,k}^{t+\Delta t}} \left\{ (P_{l,i}^{t+\Delta t} - P_{l,k}^{t+\Delta t}) h w_k + [(P_{l,i}^{t+\Delta t} - P_{l,k}^{t+\Delta t}) - g_k l_k s_{l,k}^t v_{l,k}^t] e^{\frac{-g_k \Delta t}{\rho_l h w_k}} \right\}. \quad (20)$$

Subtracting Eq. (17) from Eq. (19) yield the liquid velocity correction in the fully filled pore throat:

$$v_{l,k}'^{t+\Delta t} = \frac{\Delta t h w_k (P_{l,i}'^{t+\Delta t} - P_{l,k}'^{t+\Delta t})}{h w_k \rho_l \left(\frac{l_i}{2} + l_k + \frac{l_j}{2}\right) + \Delta t g_k \left(\frac{l_i}{2} + l_k + \frac{l_j}{2}\right)}. \quad (21)$$

Subtracting Eq. (18) from Eq. (20) yield the liquid velocity correction in the partly filled pore throat:

$$v'_{l,k,t+\Delta t} = \frac{1}{g_k l_k s_{l,k}^{t+\Delta t}} (hw_k + e^{\frac{-g_k \Delta t}{\rho_l hw_k}}) P'_{l,i,t+\Delta t}. \quad (22)$$

(5.4) Substituting the correct liquid velocity in the filled pore throat, $v_l = v_l' + v_l^*$, into Eq. (13) yields

$$\sum A_j (v'_{l,k,t+\Delta t} + v_{l,k}^{*,t+\Delta t}) = 0. \quad (23)$$

Substituting the liquid velocity correction in Eqs. (21) and (22) into Eq. (23) yields a set of linear equations for the liquid pressure correction in the each fully filled pore body. For instance, for the fully filled pore body i adjacent to pore body j and filled pore throat k , we have

$$P'_{l,i,t+\Delta t} = \frac{a_p - Q_p}{a_t}, \quad (24a)$$

$$a_p = \sum a_{t,k} P'_{l,j,t+\Delta t}, \quad (24b)$$

$$a_t = \sum a_{t,k}, \quad (24c)$$

$$Q_p = \sum A_k v_{l,k}^{*,t+\Delta t}, \quad (24d)$$

$$A_k = hw_k. \quad (24e)$$

If the pore throat k is fully filled, $a_{t,k} = A_k^2 \Delta t / (hw_k \rho_l l_k s_{l,k}^{t+\Delta t})$; if pore throat k is partly filled with liquid saturation smaller than 1, $a_{t,k} = A_k^2 [1 + \exp(-g_k \Delta t / \rho_l A_k)] / (g_k l_k s_{l,k}^{t+\Delta t})$.

By solving the linear equations, the liquid pressure correction is determined for each fully filled pore body. Then the liquid velocity correction in each filled pore throat is calculated based on Eqs. (21) and (22). In this way, the correct liquid pressure, $P_l^{t+\Delta t} = P_l^{*,t+\Delta t} + P_l'^{t+\Delta t}$, for each fully filled pore body and the correct liquid velocity, $v_l^{t+\Delta t} = v_l^{*,t+\Delta t} + v_l'^{t+\Delta t}$, for each filled pore throat are obtained.

(5.5) The guessed liquid pressure in each fully filled pore body is updated to equal to the correct liquid pressure gained in the step (5.4), i.e., $P_l^{*,t+\Delta t} = P_l^{t+\Delta t}$. Repeat from steps (5.2) until the prescribed convergence criteria are satisfied.

(6) Repeat the steps (2)–(5) until all menisci become static.

To simulate the observed capillary instability induced gas-liquid displacement in the pore network, the initial liquid pressure at time $t = t_0$ in each filled pore is needed, which, however, cannot be obtained experimentally. To get the initial condition, the following method is employed. Based on the visualization image, we can get the liquid velocity and volume in each filled pore at time $t = t_0 - \Delta t$. The liquid volume in each partially filled pore throat, e.g., pore throat j , at time $t = t_0$ is determined as $V_{l,j}^{t_0} = V_{l,j}^{t_0-\Delta t} - v_{l,j}^{t_0-\Delta t} \Delta t$. Then liquid volume, liquid pressure, and liquid velocity in each filled pore at time $t = t_0$ can be determined based on the algorithm mentioned above, and are taken as the initial conditions.

To validate the developed model, we first simulate the refilling of pores with liquid shown in Fig. 2. However, we just focus on the process from stages VI to VII, since the wettability of pore bodies are unknown. Although during this process meniscus A is in pore body 7, the adjacent pore throats 6 and 8 have very similar contact angle (40.5° and 41.7° , respectively), Fig. 2. Hence, the contact angle of pore body 7 is taken as the averaged value of these two adjacent pore throats. The contact angle of pore throat 2 is 27.5° . The calculated speed of the moving meniscus A agrees well with the experimental data; see the blue line in Fig. 3(a).

The developed pore network model is also employed to simulate the bubble movement shown in Fig. 1. The modeling and experimental results are compared in Fig. 5. Only the top right zone of the pore network (the zone marked by the red box in Fig. 1) is shown in the experimental images.

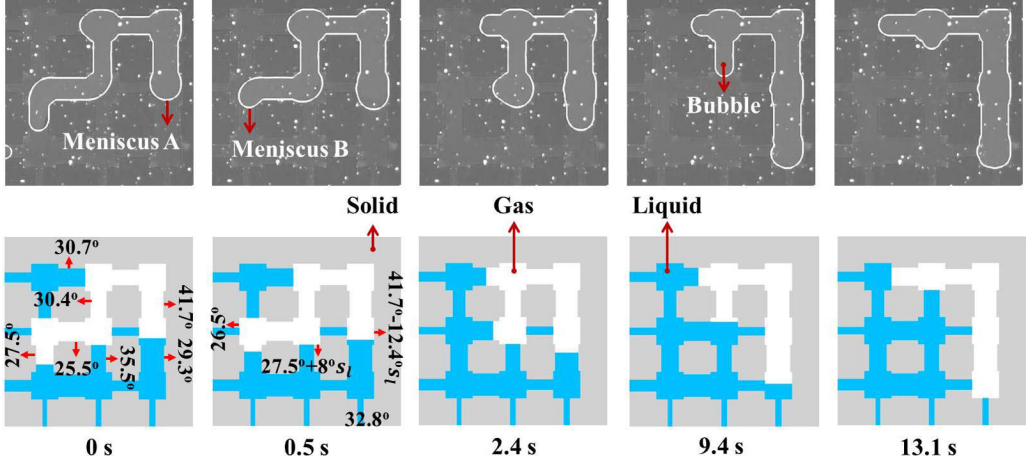


FIG. 5. Bubble movement in the top right zone of the pore network (i.e., the zone marked by the red box in Fig. 1); top: experiment; bottom: pore network model. The pore contact angles needed in the pore network model are also shown.

In the modeling images, the solid, liquid, and gas are shown in dark, gray, and white, respectively. In the model, the gas pressure in the bubble is assumed to be uniform and equal to the atmospheric pressure.

The contact angles of pores needed in the model are also shown in Fig. 5. The contact angles of pore bodies are set based on the contact angles of the neighboring pore throats. It should be noted that the contact angles in the pore throats adjacent to the same pore body can be different, which indicates the nonuniformity of the wettability of the pore body. In the present model, if the maximum difference of contact angles in the pore throats adjacent to the same pore body is more than 7° , the wettability of the pore body is considered to be nonuniform; then a linear relationship between contact angle θ and liquid saturation s_l is used to describe the wettability of the pore body, Fig. 5. If the maximum difference of contact angles in the pore throats adjacent to the same pore body is less than 7° , the contact angle of the pore body is considered to be uniform and is equal to the average of contact angles of the adjacent pore throats, Fig. 5.

As shown in Fig. 5, the bubble movement predicted by the pore network model agrees well with the experimental results. It takes a relatively long time for meniscus B to enter the pore body at the center of the pore network (see images of $t = 2.4$ and 9.4 s). The main reason is that when meniscus B meets the residual liquid in the pore body, its curvature radius, r_i , increases, thereby leading to the reduced capillary pressure and hence the increased liquid pressure, which in turn hinders the movement of meniscus B. The good agreement between the modeling and experimental results in terms of meniscus moving speed [Fig. 3(a)] and variation of the liquid phase distribution (Fig. 5) demonstrates the effectiveness of the developed pore network model.

IV. DISCUSSION

By using the pore network model developed in Sec. III, we take the bubble movement shown in Fig. 5 as an example to illustrate the impacts of the inertial forces on the gas-liquid displacement in porous media. To do this, the bubble movement is simulated by the pore network models with the inertial effect (PNMwI) and without the inertial effect (PNMwoI). The surface tension value is varied between $0.001\sigma_f$ and $50\sigma_f$. Because of this variation, the gas bubble can move at different speeds (the higher the surface tension, the faster the bubble moves). Here, $\sigma_f = 0.0221 \text{ Nm}^{-1}$ is the reference surface tension, which is the surface tension of ethanol used in our experiments. In all simulations, the initial conditions are the same, mimicking the experiment (e.g., see Fig. 5). The

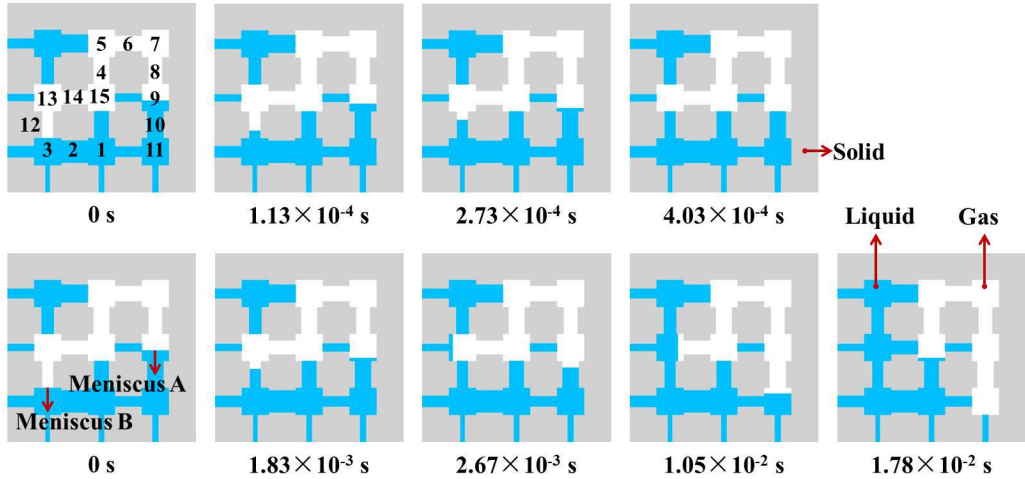


FIG. 6. Evolution of the gas bubble in the transformed pore network at the surface tension of $46.5\sigma_f$ obtained by the pore network model without (top) and with (bottom) the inertial forces.

average speed of the receding meniscus is calculated from the distance travelled divided by the associated time. The average speed, $v_{r,wi}$, obtained from PNMwI simulations is used to determine the Weber number ($\frac{\rho v_{r,wi}^2 h}{\sigma}$) and the capillary number ($\frac{\mu v_{r,wi}}{\sigma}$), as well as the Reynolds number ($\frac{\rho v_{r,wi} h}{\mu}$). The average speed of the receding meniscus is used because more than one advancing meniscus can get involved during the bubble movement (e.g., Fig. 5).

All the pores in the microfluidic pore network have a rather small height ($50\ \mu\text{m}$). Even if the surface tension is increased by a factor of 50, both the capillary number (1.9×10^{-5}) and the Weber number (1.6×10^{-5}) are rather small. Hence, the capillary forces dominate the bubble movement, and the inertial and viscous forces can be neglected. To this end, the final bubble configuration predicted by the PNMwI and the PNMwoI are almost the same as that in Fig. 5. The time used to determine the average speed of the receding meniscus is the period from the initial moment to the final stable moment.

In order to elucidate the role of the inertial forces, we change the pore height to $500\ \mu\text{m}$, and contact angle values of the silicon surfaces in all pores to 40° . In addition, the widths of pore throats 12, 14, 8, and 10 are changed to 0.4, 0.5, 0.5, and 0.6 mm, respectively (the numbers of pores are illustrated in Fig. 6 as well as in Fig. 2). For bubble movement in this transformed pore network, there is only one advancing meniscus (A) and only one receding meniscus (B). We find that the final stable bubble configuration predicted by the PNMwI and the PNMwoI are different when surface tension is equal to or larger than $46.5\sigma_f$ (the Weber number is 0.085), Fig. 6. The time steps used in the PNMwoI and PNMwI simulations are $3.33 \times 10^{-8}\ \text{s}$ and $1.66 \times 10^{-6}\ \text{s}$, respectively. The average speed of the receding meniscus is the distance from the initial point to the entrance of pore body 13 divided by the time for the receding meniscus moving through this distance. In the PNMwoI, when the advancing meniscus, initially in pore body 9, reaches the entrance of pore throat 10, and the receding meniscus reaches the entrance of the pore body 13, then the bubble halts. The reason is that the capillary pressure of the moving meniscus in pore throat 10 is larger than that of pore body 13. However, because of the inertial forces in the PNMwI, the advancing meniscus invades pore throat 10 and pore body 11, and the receding meniscus enters pore body 13 and pore throat 14; see images at time $2.67 \times 10^{-3}\ \text{s}$, $1.05 \times 10^{-2}\ \text{s}$, and $1.78 \times 10^{-2}\ \text{s}$ at the bottom of Fig. 6.

When the Weber number is smaller than the critical value 0.085, the final bubble configuration in the transformed pore network is the same for PNMwoI and PNMwI. However, we observe the menisci oscillation in PNMwI when the Weber number is smaller than but close to the critical value

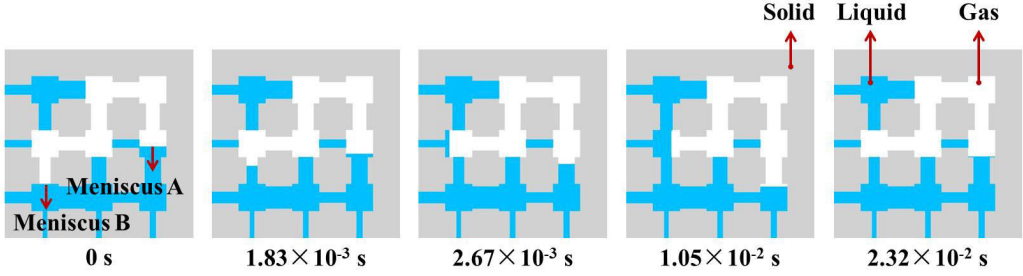


FIG. 7. Evolution of the gas bubble in the transformed pore network at the surface tension of $45\sigma_f$ obtained by the pore network model with the inertial forces.

0.085 (this menisci oscillation cannot be predicted by the PNW_woI). When the Weber number is 0.082, the advancing meniscus can enter pore throat 10 and pore body 11, and the receding meniscus can enter pore body 13, because of the inertial forces in PNWwI; see images at the time of 2.67×10^{-3} and 1.05×10^{-2} s in Fig. 7. But, the inertial forces cannot overcome the capillary forces. Eventually, the advancing meniscus moves back to pore body 9, and the receding meniscus moves back to the entrance of pore throat 12; see the image at time of 2.32×10^{-2} s in Fig. 7.

To elucidate the role of inertial forces on the gas-liquid two-phase displacement, we compare the average speed of the receding meniscus moving from the initial point to the entrance of pore body 13 obtained from PNMwI and PNMwoI, $v_{r,wi}$ and $v_{r,woi}$. The Weber number is varied by changing the surface tension from $0.001 \sigma_f$ to $45 \sigma_f$. The Weber number is varied from 5.1×10^{-5} to 8.2×10^{-2} , Reynolds number from 0.021 to 174.1, and the capillary number from 4.7×10^{-4} to 2.5×10^{-3} . In PNMwoI, the average speed of the receding meniscus is

$$v_{woi} \sim \frac{\sigma}{\mu_l}. \quad (25)$$

In PNMwI, the average speed of the receding meniscus can be expressed based on the definition of the Weber number mentioned above:

$$v_{wi} = \sqrt{\frac{\sigma We}{\rho_l h}}. \quad (26)$$

From Eqs. (25) and (27), we can get

$$\frac{v_{wi}}{v_{woi}} \sim \sqrt{\frac{\sigma We}{\rho_l h}} \bigg/ \frac{\sigma}{\mu_l} = \sqrt{\frac{\mu_l We}{\rho_l h \sigma}} = \sqrt{\frac{We}{\rho_l h v_{woi}}}, \quad (27)$$

and Eq. (27) indicates that

$$\frac{v_{wi}^2}{v_{woi}} \sim We. \quad (28)$$

Equation (28) shows that v_{wi}^2/v_{woi} is a linear function of We , i.e., $v_{wi}^2/v_{woi} = c_1 + c_2 We$, which agrees well with the pore network simulation results shown in Fig. 8. Our calculations show that the coefficients c_1 and c_2 depend on the pore network structure and wettability as well as on the physical properties of the liquid (e.g., density and viscosity).

V. SUMMARY AND CONCLUSIONS

In summary, we report experimentally that during evaporation of a microfluidic pore network composed of pore throats and pore bodies, the pores occupied by gas can be refilled with liquid, snapping off a gas bubble, which then moves as long as a stable configuration is reached. The phenomena of the pore refilling and the bubble formation and movement are induced by the

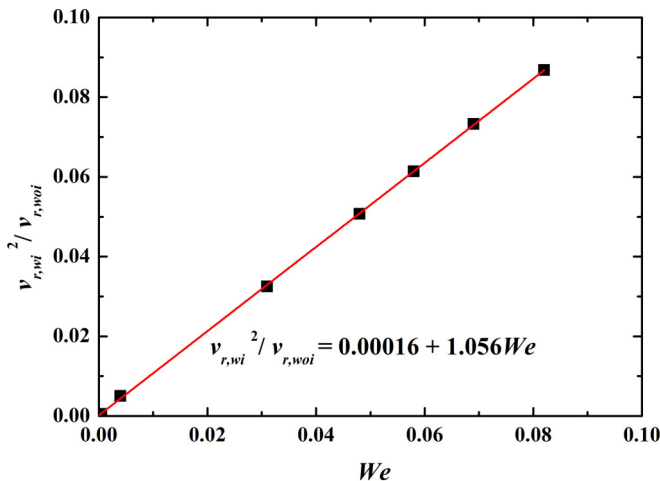


FIG. 8. Variation of the $v_{r,wi}^2/v_{r,woi}$ with the Weber number for gas-liquid displacement in the transformed pore network. $v_{r,wi}$ and $v_{r,woi}$ are the average speed of the receding meniscus obtained from the pore network models with and without the inertial effect, respectively. We is the Weber number. The fitted line is also shown.

capillary instability due to the heterogeneity in wettability. Such capillary instability induced gas-liquid displacement is explained in detail based on the optical images acquired from visualization experiment. We find that the capillary valve effect, which hinders the menisci movement, can be suppressed by the residual liquid in the pore body. The residual liquid in a pore body and the menisci inside the neighboring pore throat can be connected by corner liquid films. The speed of the capillary instability induced moving menisci depends on the interaction between the advancing and the receding menisci, i.e., through the liquid-filled pores (pore flow) or the corner liquid films (corner flow). The moving menisci induced by the capillary instability with the pore flow have a higher speed than those with the corner flow. To form the gas ganglion, the threshold pressure for the receding meniscus to refill a pore body connected to at least two empty pore throats should be surmounted by the driving force, i.e., the difference in capillary forces between the advancing and receding menisci.

A pore network model that accounts for not only the capillary and viscous forces but also the inertial forces is developed to predict the experimentally observed capillary instability induced gas-liquid displacement. The pore network simulation results agree well with the experimental data, validating the effectiveness of the developed model. We find that the ratio of the square of the average meniscus moving speed predicted by the pore network model with inertial effect to the average meniscus moving speed predicted by the model without the inertial effect is a linear function of the Weber number. When the Weber number exceeds a critical value, more pores are invaded by the gas-liquid interface in the pore network model with the inertial effect than in the model neglecting the inertial effect. The developed pore network model opens up a route for better understanding of the role of inertial forces in two-phase transport in porous media. We believe that unveiling, both experimentally and numerically, the capillary instability effect paves the way toward fundamental understanding of the two-phase transport phenomena in porous media.

ACKNOWLEDGMENTS

The authors are grateful for the support from the National Key Research and Development Program of China (No. 2018YFC1800600), the National Natural Science Foundation of China (No. 51776122), and the Alexander von Humboldt Foundation.

- [1] T. M. Shaw, Drying as An Immiscible Displacement Process with Fluid Counterflow, *Phys. Rev. Lett.* **59**, 1671 (1987).
- [2] T. Metzger and E. Tsotsas, Viscous stabilization of drying front: Three-dimensional pore network simulations, *Chem. Eng. Res. Des.* **86**, 739 (2008).
- [3] A. G. Yiotis, D. Salin, E. S. Tajar, and Y. C. Yortsos, Drying in porous media with gravity-stabilized fronts: Experimental results, *Phys. Rev. E* **86**, 026310 (2012).
- [4] N. Vorhauer, E. Tsotsas, and M. Prat, Temperature gradient induced double stabilization of the evaporation front within a drying porous medium, *Phys. Rev. Fluids* **3**, 114201 (2018).
- [5] S. Biswas, P. Fantinel, O. Borgman, R. Holtzman, and L. Goehring, Drying and percolation in correlated porous media, *Phys. Rev. Fluids* **3**, 124307 (2018).
- [6] O. Chapuis and M. Prat, Influence of wettability condition on slow evaporation in two-dimensional porous media, *Phys. Rev. E* **75**, 046311 (2007).
- [7] L. Xu, S. Davies, A. B. Schofield, and D. A. Weitz, Dynamics of Drying in 3D Porous Media, *Phys. Rev. Lett.* **101**, 094502 (2008).
- [8] N. Shokri and M. Sahimi, Structure of drying fronts in three-dimensional porous media. *Phys. Rev. E* **85**, 066312.(2012).
- [9] J. Thiery, S. Rodts, D. A. Weitz, and P. Coussot, Drying regimes in homogeneous porous media from macro-to nanoscale, *Phys. Rev. Fluids* **2**, 074201 (2017).
- [10] E. Keita, P. Faure, S. Rodts, and P. Coussot, MRI evidence for a receding-front effect in drying porous media, *Phys. Rev. E* **87**, 062303 (2013).
- [11] M. Prat, Pore network models of drying, contact angle, and film flows, *Chem. Eng. Technol.* **34**, 1029 (2011).
- [12] T. Defraeye, Advanced computational modelling for drying processes – A review, *Appl. Energy* **131**, 323 (2014).
- [13] F. Moebius and D. Or, Inertial forces affect fluid front displacement dynamics in a pore-throat network model, *Phys. Rev. E* **90**, 023019 (2014).
- [14] R. Wu, A. Kharaghani, and E. Tsotsas, Two-phase flow with capillary valve effect in porous media, *Chem. Eng. Sci.* **139**, 241 (2016).
- [15] R. Wu, A. Kharaghani, and E. Tsotsas, Capillary valve effect during slow drying of porous media, *Int. J. Heat Mass Transfer* **94**, 81 (2016).
- [16] P. Panizza, H. Algaba, M. Postic, G. Raffy, L. Courbin, and F. Artzner, Order-Disorder Structural Transitions in Mazes Built by Evaporation Drops, *Phys. Rev. Lett.* **121**, 078002 (2018).
- [17] Y. Edery, S. Berg, and D. Weitz, Surfactant Variations in Porous Media Localize Capillary Instabilities During Haines Jumps. *Phys. Rev. Lett.* **120**, 028005 (2018).
- [18] C. Odier, B. Levache, E. Santanach-Carreras, and D. Bartolo, Forced Imbibition in Porous Media: A Fourfold Scenario, *Phys. Rev. Lett.* **119**, 208005 (2017).
- [19] B. Zhao, C. W. MacMinn, and R. Juanes, Wettability control on multiphase flow in patterned microfluidics, *Proc. Natl. Acad. Sci.* **113**, 10251 (2016).
- [20] R. T. Armstrong and S. Berg, Interfacial velocities and capillary pressure gradients during Haines jumps, *Phys. Rev. E* **88**, 043010 (2013).
- [21] C. A. Reynolds, H. Menke, M. Andrew, M. J. Blunt, and S. Krevor, Dynamic fluid connectivity during steady state multiphase flow in a sandstone, *Proc. Natl. Acad. Sci.* **114**, 8187 (2017).
- [22] S. S. Datta, J. Dupin, and D. A. Weitz, Fluid breakup during simultaneous two-phase flow through a three-dimensional porous medium, *Phys. Fluids* **26**, 062004 (2014).
- [23] D. G. Avraam and A. C. Payatakes, Flow regimes and relative permeabilities during steady-state two-phase flow in porous media, *J. Fluid Mech.* **293**, 207 (1995).
- [24] See Supplemental Material at <http://link.aps.org/supplemental/10.1103/PhysRevFluids.5.104305> for more details on visualization experiments and pore network models.
- [25] W. Tao, H. Zhong, X. Chen, Y. Selami, and H. Zhao, A new fitting method for measurement of the curvature radius of a short arc with high precision, *Meas. Sci. Technol.* **29**, 075014 (2018).
- [26] E. Atefi, J. A. Mann, and Jr, H. Tavana, A robust polynomial fitting approach for contact angle measurements, *Langmuir* **29**, 5677 (2013).

- [27] E. F. Ethington, Interfacial contact angle measurements of water, mercury, and 20 organic liquid on quartz, calcite, biotite, and Ca-montmorillonite substrates (U. S. Geological Survey, Report No. 90-409, 1990).
- [28] Y. Wang and Z. Wang, Droplets wetting and evaporating on ethanol-philic micro-structured surfaces, *Int. J. Heat Mass Transfer* **119**, 704 (2018).
- [29] S. J. Spencer, G. T. Andrews, and C. G. Deacon, Contact angle of ethanol–water solutions on crystalline and mesoporous silicon, *Semicond. Sci. Technol.* **28**, 055011 (2013).
- [30] H. Wong, S. Morris, and C. J. Radke, Three-dimensional menisci in polygonal capillaries, *J. Colloid Interface Sci.* **148**, 317 (1992).
- [31] F. Schellenberger, N. Encinas, D. Vollmer, and H. J. Butt, How Water Advances on Superhydrophobic Surfaces, *Phys. Rev. Lett.* **116**, 096101 (2016).
- [32] C. Semperebon, S. Herminghaus, and M. Brinkmann, Advancing modes on regularly patterned substrates, *Soft Matter* **8**, 6301 (2012).
- [33] R. P. Mayer and R. A. Stone, Mercury porosimetry – breakthrough pressure for penetration between packed spheres, *J. Colloid Sci.* **20**, 893 (1965).
- [34] H. M. Princen, Capillary phenomena in assemblies of parallel cylinders, *J. Colloid Interface Sci.* **30**, 69 (1969).
- [35] T. C. Ransohoff, P. A. Gauglitz, and C. J. Radke, Snap-off of gas bubbles in smoothly constricted noncircular capillaries, *AIChE J.* **33**, 753 (1987).
- [36] C. Chen, P. Duru, P. Joseph, S. Geoffroy, and M. Prat, Control of evaporation by geometry in capillary structures. From confined pillar arrays in a gap radial gradient to phyllotaxy-inspired geometry, *Sci. Rep.* **7**, 15110 (2017).
- [37] N. Ichikawa, K. Hosokawa, and R. Maeda, Interface motion of capillary-driven flow in rectangular microchannel, *J. Colloid Interface Sci.* **280**, 155 (2004).
- [38] R. Wu, T. Zhang, C. Ye, C. Y. Zhao, E. Tsotsas, and A. Kharaghani, Pore network model of evaporation in porous media with continuous and discontinuous corner films, *Phys. Rev. Fluids* **5**, 014307 (2020).
- [39] J. F. Canny, A computation approach to edge detection, *IEEE Trans. Pattern Anal. Mach. Intell.* **8**, 679 (1986).
- [40] W. Gander, G. H. Golub, and R. Strebler, Least squares fitting of circles and ellipses, *BIT Numer. Math.* **34**, 558 (1984).
- [41] N. Chernov and C. Lesort, Least squares fitting of circles, *J. Math. Imaging Vis.* **23**, 239 (2005).

Correction: A discrepancy in the presentation of the last two author names was missed during the editorial processing and production cycle and has been rectified.